Three-Dimensional Printing of Elastomeric, Cellular Architectures with Negative Stiffness

Eric B. Duoss, Todd H. Weisgraber, Keith Hearon, Cheng Zhu, Ward Small IV, Thomas R. Metz, John J. Vericella, Holly D. Barth, Joshua D. Kuntz, Robert S. Maxwell, Christopher M. Spadaccini,* and Thomas S. Wilson**

Three-dimensional printing of viscoelastic inks to create porous, elastomeric architectures with mechanical properties governed by the ordered arrangement of their sub-millimeter struts is reported. Two layouts are patterned, one resembling a "simple cubic" (SC)-like structure and another akin to a "face-centered tetragonal" (FCT) configuration. These structures exhibit markedly distinct load response with directionally dependent behavior, including negative stiffness. More broadly, these findings suggest the ability to independently tailor mechanical response in cellular solids via micro-architected design. Such ordered materials may one day replace random foams in mechanical energy absorption applications.

1. Introduction

Nature controls material properties via intricate assembly and structural organization of matter, often with embedded porosity. Naturally occurring cellular solids, such as wood, cancellous bone, and cork, are lightweight yet mechanically robust. The most widespread cellular solids are foams. Solid foams are typically selected for a given application for their energy absorption or cushioning properties, though they are increasingly employed for their thermal, electrical, or other functional properties.[1] Foams consist of a pseudo-stochastic arrangement of material and void, which can lead to local structural heterogeneities and non-uniform properties. Consequently, their mechanical properties are often tuned by changing the material and/or the degree of porosity (i.e., the relative density), since structural control is difficult. Due to their pseudo-stochastic nature, foams do not lend themselves well to predictive modeling of their mechanical properties or aging behavior. Moreover, it is challenging to produce foams with well-controlled directional properties.

Cellular solids also include highly ordered architectures which offer the opportunity to engineer the mechanical response by carefully controlling the structure[2] (rather than composition) to create so-called mechanical metamaterials.[3,4] For example, lattice structures may be designed such that they are stretch-dominated and, hence, offer superior stiffness and strength for a given relative density versus their bend-dominated counterparts (including foams).[5,6] Extremal properties are possible in cellular structures, where "extremal" denotes the composite property exceeds that of the constituents.[7] For example, idealized unit cells possess a negative Poisson's ratio such that they exhibit transverse contraction (or expansion) under longitudinal compressing (or stretching).[8–11] Negative stiffness materials exhibit a reversal of the restoring force that occurs when materials are loaded, that is, the load-deformation curve possesses a negative slope.[7,12–14] Negative stiffness is an inherently useful property. For example, helmet inserts with negative shear stiffness could be designed so that forces from glancing blows are not transmitted to the user. Yet, a pressing challenge lies in designing and manufacturing such structures, especially with microscale features in periodic layouts with deterministic properties.

Additive manufacturing is especially well-suited to create such complex, 3D structures with engineered properties without the need for expensive tooling, dies, or fixtures and with minimal post-processing.[15] 3D printing processes, such as direct ink writing (DIW),[16] have garnered significant attention recently for their ability to enable and improve many emerging technologies. For example, 3D printing has been employed to create a wide range of biological materials such as tissue scaffolds,[17,18] microvascular networks,[19–21] self-healing materials,[22] and artificial organs.[23] Micro- and nanoscale functional materials have also been patterned with 3D printing; examples include photonic crystals,[24–27] metamaterials,[28,29] microelectrodes,[30] antennas,[31] and batteries.[32] In addition, 3D patterning approaches have been harnessed to create structures with unique mechanical properties, such as microscale truss structures,[33,34] ultralight metallic microlattices,[35] and hollow ceramic nanostructures.[36]

Here, we report 3D printing of viscoelastic inks to create porous, elastomeric architectures with mechanical properties governed by the ordered arrangement of their sub-millimeter

E. B. Duoss, T. H. Weisgraber, K. Hearon, C. Zhu, W. Small IV, T. R. Metz, J. J. Vericella, H. D. Barth, J. D. Kuntz, R. S. Maxwell, C. M. Spadaccini, T. S. Wilson
Lawrence Livermore National Laboratory
7000 East Avenue, Livermore, CA 94551, USA
E-mail: duoss1@llnl.gov; spadaccini2@llnl.gov; wilson97@llnl.gov

DOI: 10.1002/adfm.201400451

struts. We patterned two layouts, one resembling a "simple cubic" (SC)-like structure and another akin to a "face-centered tetragonal" (FCT) configuration. These structures exhibit markedly distinct load response with directionally dependent behavior, including negative stiffness. More broadly, our findings suggest the ability to independently tailor mechanical response in cellular solids via micro-architected design. Such ordered materials may one day replace stochastic foams in many energy absorption applications. To our knowledge, this report is the first time that 3D printing has been harnessed to pattern highly flexible and stretchable 3D periodic structures with tailored mechanical properties, including negative stiffness.

2. Results and Discussion

The combination of micro-architected design and 3D printing offers the ability to create ordered structures with highly controlled and predictable properties. Our 3D printing approach offers exquisite control over the structural arrangement of material and void, which enables the construction of cellular structures with designed mechanical properties. In this fabrication process, we deposit a silica-filled, polydimethylsiloxane paste, or "ink," from a micronozzle onto a substrate in a programmed pattern using a three-axis, linear positioning system. The ink is pressurized and extruded in filamentary form onto a substrate that is translated within the horizontal plane (x, y axes) while the printhead is positioned vertically (z-axis) as a structure is built up layer-by-layer (**Figure 1**a and Video S1 in the Supporting Information). We match the ink volumetric flow rate to the substrate translation speed to obtain patterned feature sizes approximately equal to the nozzle diameter.

The ink's rheological properties govern its ultimate printability for this room temperature patterning process. The siloxane-based ink material exhibits non-Newtonian flow behavior including shear rate dependent viscosity (see Figure S1 in the Supporting Information). The apparent viscosity lowers as shear rate increases, enabling ink to flow out of micronozzles (e.g., inner diameters = 100–610 μm) at reasonable pressures (e.g., 70–700 kPa) for typical print-speeds (e.g., 1–20 mm s^{-1}). Under these conditions, a typical pattern program consisting of 8 layers in the z-direction, 75 mm × 75 mm areal footprint in the xy plane, and a filament center-to-center spacing of 1220 μm requires ≈1 h total print time. To determine the longest possible print time of the uncured ink material after preparation, we examined the time-dependent rheology of the ink at room temperature (≈23 °C) (see Figure S2 in the Supporting Information). The ink displays a gradual rise in both apparent viscosity and dynamic storage modulus (G') until undergoing a steep increase at 14 h. From printing test observations, we find the ink can be used for 3D printing for up to 12 h after preparation. To account for the gradual viscosity increase after preparation, we employ a controlled displacement dispenser (instead of a controlled pressure system), which yields uniform filament cross-sections throughout the duration of a print. The ink exhibits stress-dependent shear storage (G') and loss (G'') moduli with more liquid-like behavior ($G'' > G'$) under large oscillatory stresses (>800 Pa) and solid-like "yielding" behavior

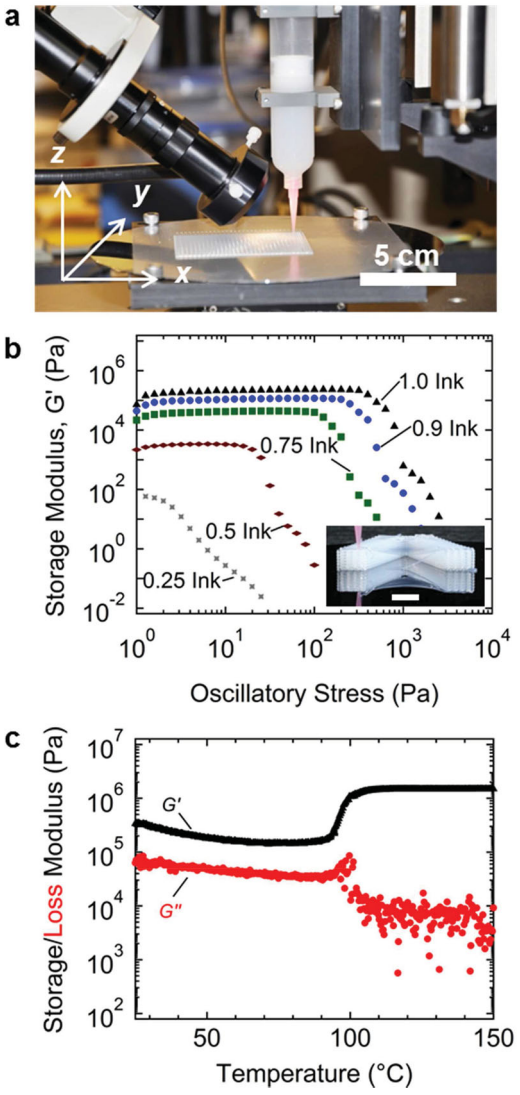

Figure 1. 3D printing process and ink rheology. a) Photograph of the 3D printing apparatus. b) Storage modulus (G') versus oscillatory stress for the silica-filled ink material (labeled "1.0 Ink") and mixtures of the filled ink diluted with unfilled siloxane resin (prefix indicates weight fraction of filled ink material in the mixture). The plateau storage modulus and yield stress decrease as the filled ink material is diluted. Inset is a photograph (scale bar = 1.0 cm) of a "V"-shaped test structure printed with filled ink ("1.0 Ink") where printed filaments span unsupported distances of >2 cm. c) Temperature-dependence of storage and loss (G'') moduli during a thermal ramping condition indicating the ink begins curing at ≈90 °C with minimal thermal softening.

at lower oscillatory stresses (see Figure S1 in the Supporting Information). This yield stress decreases with decreasing filler concentration as shown in Figure 1b, where silica-filled ink is diluted with unfilled siloxane resin. Likewise, the viscosity decreases as the concentration of the filled ink material is lowered (see Figure S3 in Supporting Information). As filler concentration decreases, the storage modulus decreases, creating a condition where printed filaments will collapse and rendering 3D printing impossible at concentrations of 50% filled ink and below (see Figure S3 in Supporting Information). We note

that, in this printing process, ink flow is facilitated by being above the yield stress at high shear rates (i.e., a condition that exists in the vicinity of the nozzle wall). After deposition and in the absence of further significant shear, the ink becomes more solid-like (i.e., a condition below the yield stress where $G'>>G''$), which enables shape retention.

In practice, we find the undiluted ink rapidly solidifies as it exits the nozzle, which enables filaments to span unsupported regions greater than 2 cm (Figure 1b, inset). Hence, porous lattice structures can be built up in a layer-by-layer fashion by spanning gaps in the underlying layer(s). A distinguishing feature of this 3D printing process is that the ink is not cured during a build sequence. Instead, the as-patterned lattice is thermally cured in a post-printing step by heating to 150 °C to form a chemically cross-linked, filler reinforced rubber. A post-printing cure step is an important feature because layers inter-diffuse post printing, resulting in a slight interlayer "overlap" between filaments and effectively removing any distinct interface on cure. To determine if thermally induced softening occurs while heating to the cure temperature, we examined G' and G'' of the uncured ink in the low strain limit (≤0.30%) with increasing temperature at 2 °C min^{-1} from 25 to 150 °C. The ink material remains solid-like as temperature is ramped to 150 °C with $G' > G''$ in all cases (Figure 1c). Thus, we expect the printed shape will be preserved during the thermal treatment (i.e., no unintended deformation due to thermal softening).

To explore the feasibility of controlling mechanical properties via micro-architected design, we patterned two 3D micro-architectures. The first pattern is a SC-like structure schematically illustrated in **Figure 2**a. In this structure, filaments within each horizontal layer in the *xy* plane run parallel to each other with

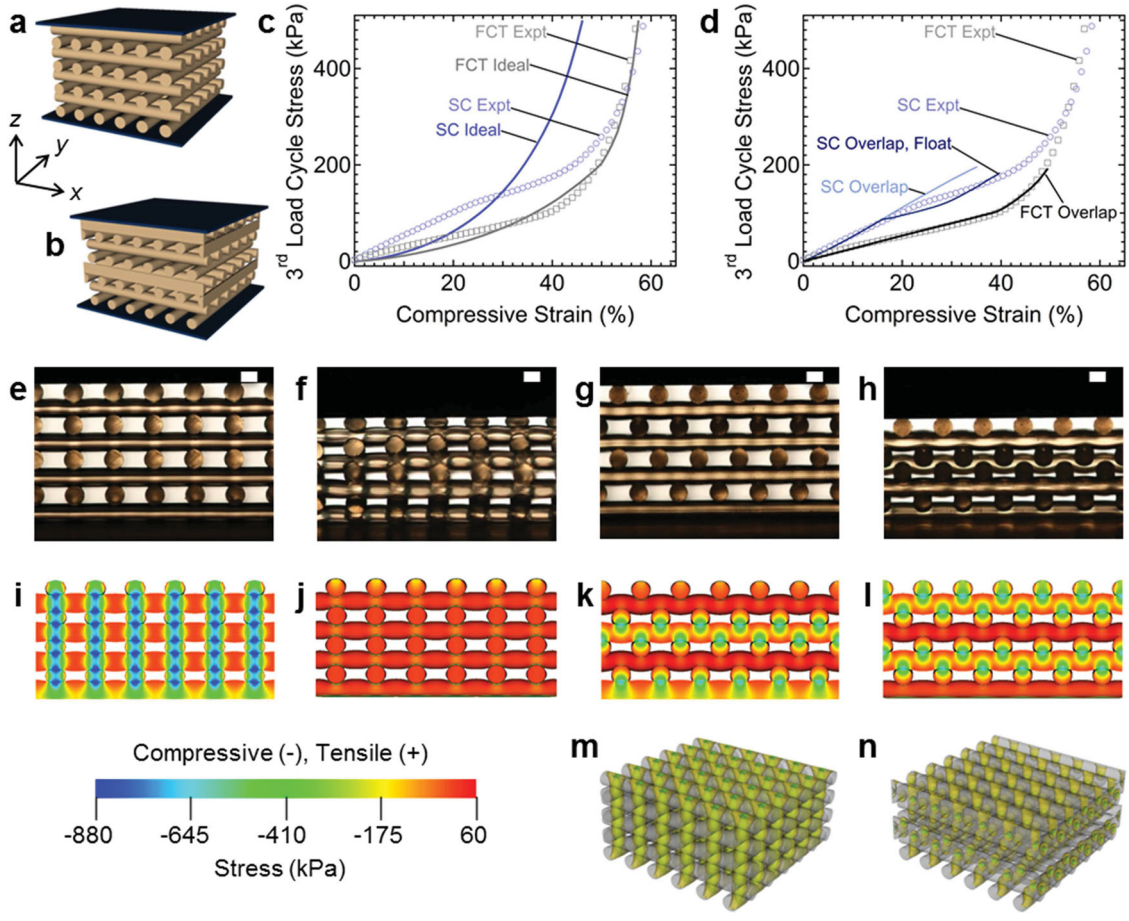

Figure 2. Architecture-dependent uniaxial compression behavior. a) Schematic illustrations of simple cubic (SC) and b) face centered tetragonal (FCT) structures. The top and bottom plates represent the test fixture. c) 3rd load cycle engineering stress versus engineering strain for uniaxial compression. The plot compares experimental results ("Expt") to finite element (FE) simulations for idealized structures ("Ideal") that do not possess any interlayer overlap and are symmetry constrained. The SC structure shows higher stress for a given strain for both experiment and simulation. d) FE simulation agreement with experiment improves by incorporating interlayer overlap ("Overlap") and a top plate that is allowed to laterally float ("Overlap, Float"). Cross-sectional images in the *xz*-plane are shown of a printed SC structure under e) 0% and f) 25% compression and of a printed FCT structure under g) 0% and h) 25% compression. Scale bars are 500 μm for (e–h). Cross-sections in the *xz*-plane from 3D FE simulations showing stress in an SC structure i) bisected through filaments in the *x*-direction and j) with the cross-section shifted by half the pitch in the *y*-direction from (i), and in k) an FCT structure bisected through filaments in *x*-direction and l) with the cross-section shifted by half the pitch in the *y*-direction from (k). Color-scale shows compressive stress (negative) and tensile stress (positive). A continuous load column forms in the SC structure whereas the load path in the FCT structure is staggered. This behavior is confirmed by isometric projections showing stress iso-surfaces for m) SC and n) FCT structures under 25% compression.

a predetermined center-to-center spacing or pitch. The subsequent layer is oriented orthogonal to the previous layer with every alternating layer in the *z*-direction being overlaid. The second pattern is the FCT-like structure shown in Figure 2b. In this pattern, every other layer is shifted orthogonally to the filament direction by half the pitch relative to two layers below it, which causes the structure to repeat every four layers. For the results shown here, 8-layer SC and FCT structures are printed with a pitch that is twice the nozzle diameter (i.e., 1,220 μm pitch for the 610 μm inner diameter nozzles used in this work). To facilitate visualization, 3D reconstructions of printed parts obtained using Synchrotron Radiation micro-Tomography (SRμT) performed on the SC and FCT architectures are shown in Videos S2, S3 in the Supporting Information. Every layer is patterned with a slight overlap in the z-direction to ensure good adhesion between layers. The final, cured parts have relative densities (or volume fractions) of ~0.52 for both the SC and FCT pattern programs due to interlayer overlap. For reference, the relative density of the ideal structures, which we define as filaments of perfect circular cross-section with point contacts between layers, is 0.39.

To determine the effect of micro-architecture on performance, we performed uniaxial compression tests as well as shear tests under pre-compression on the SC and FCT structures. These lattice structures exhibit complex load-deformation behavior with the ability to individually tailor response based upon structure. Under uniaxial compression, the SC lattice structure exhibits a higher compressive engineering stress for a given engineering strain than its FCT counterpart (experimental data shown in Figure 2c,d). Please note, we plot the 3rd cycle loading data to remove the effect of strain history dependent stress-softening (Mullins effect) known to occur in rubbers.[37] For completeness, the loading-unloading data for all three cycles for both SC and FCT structures is shown in Figure S4 in the Supporting Information. To observe the structural deformation, we exposed cross-sections of SC and FCT structures and imaged under increasing levels of compression. Figure 2e–h shows images of the SC and FCT structures at 0% and 25% compressive strain (see Figure S5 in the Supporting Information for images in 5% strain increments for 0–25% strain). In addition, SRμT 3D reconstructions of printed SC and FCT architectures under 25% compression are shown in Videos S4, S5 in the Supporting Information. It is apparent that the SC structure becomes unstable and buckles under the compressive load at ~15–20% strain. In contrast, the FCT structure exhibits little noticeable lateral deformation under compression, since filaments are guided into the interstitial space in the underlying layers. As compression continues to >50% strain, both structures encounter the lock-up or densification regime characterized by a dramatic upturn in the stress-strain curve.

To better understand the load-deformation behavior of these materials, we developed a finite element model for both micro-architectures. Our simulation accurately predicts that the SC design will possess a higher compressive engineering stress than FCT for a given engineering strain for both idealized (Figure 2c) and overlapped structures (Figure 2d). The origin of this effect is depicted in the stress distribution maps of the idealized structures illustrated in Figure 2i–l. Note the cross-sections shown in Figure 2i,k bisect through filaments running in the *x*-direction while the accompanying cross-sections in Figure 2j,l are shifted in the *y*-direction by half the filament center-to-center spacing. Within the SC structure, columnar stress concentration paths develop at each of the interlayer filament intersections, which are evenly spaced on a square grid in the *xy*-plane (Figure 2i). Virtually none of the load is distributed to the space between columns (Figure 2j). While initially stiff, these load-carrying columns are inherently unstable and prone to buckling, which eventually leads to the softening behavior observed in the experimental data. Like its SC counterpart, the FCT structure concentrates stress at the interlayer filament intersections however, in contrast to SC, the FCT load path diverges at each of the intersections due to the staggered structural arrangement such that more of the structure carries the load. The 3D simulation images in Figure 2m,n and accompanying Videos S6, S7 in the Supporting Information illustrate this point by showing the development of iso-stress surfaces under uniaxial compression. It is apparent that the FCT load path is more broadly distributed than the SC columns, resulting in a lower stress response for a given level of compression.

As we have seen, compared to experiment, the simulations for the idealized structures under predict the absolute values of compressive stress at low strains and, for the SC structure, over predict stress at high strains (Figure 2c). In the idealized case, the compression simulation was performed on non-overlapping layers of filaments of circular cross-section with the constraint of purely symmetric deformation at the lateral boundaries. In reality, our structures exhibit overlap in the *z*-direction and test conditions likely violate the symmetry constraint. We attribute the higher experimental stress at low strains to overlap, which increases the solid fill fraction of the actual part versus its simulated version. At high strains, our structures are able to break their symmetry and undergo lateral displacements due to buckling. The result is a softening effect with comparatively lower experimental stress relative to simulation at strains >30%. To develop a more predictive model, we revised the simulation to incorporate interlayer overlap and free the ends by removing the symmetry constraint. We found that the revised simulation conditions offer better agreement to the experimentally observed behavior for the selected curves (Figure 2d). Moreover, relaxing the constraint on the upper plate so it can move laterally during compression further improves the agreement since it promotes the buckling behavior. Though this kind of boundary is not available in experiments, the specimens can slip with respect to the actuating surfaces to relieve the large stress and allow for softening.

To probe the uniformity of these printed micro-architectures, we measured the stress-strain response in uniaxial compression in four distinct locations in the *xy*-plane within four 75 mm × 75 mm parts for each micro-architecture and calculated the coefficient of variance under 15%, 25%, 40%, 55%, and 70% compressive strain (see Figure S6 in the Supporting Information). We attribute the higher uniformity in the FCT structure to the inherent instability that occurs in the SC structure associated with the development of the columnar load path. Nevertheless, the overall performance of both micro-architectures is extremely uniform.

To probe the shear response of both micro-architectures, we performed uni-directional and oscillatory shear measurements

on SC and FCT parts loaded under pre-compression. First, we mounted two identical structures into a shear sandwich test fixture such that the shear direction is oriented parallel (or perpendicular) to the filament direction within a given layer. Next, we pre-loaded the structures by applying increasing amounts of compressive strain. In the test layout, the outer surface of each structure remained fixed while the inner surface was sheared by a piston, either uni-directionally (for the data shown in **Figure 3**) or in an oscillatory fashion (for Videos S8, S9 in the Supporting Information). Under 25% and 40% compression, the uni-directional FCT shear response initially displays a monotonic rise in engineering shear stress with increasing engineering shear strain until it levels off with the onset of wall slip between the structure and test cell (Figure 3a).

The behavior of the SC structure under uni-directional shear is more noteworthy. Under an axial compression of 25%, the SC stress-strain response develops a negative slope at ~20% shear strain, indicating a decrease in stiffness. When compressive strain is increased to 30% and 40%, the SC structure not only displays negative slope, but the value of shear stress turns negative for a limited range of shear strain. This negative stiffness behavior is especially apparent in the oscillatory strain measurement of the SC structure shown in Video S8 in the Supporting Information. While undergoing a dynamic strain sweep under controlled stress, the SC structure under 25% pre-compression clearly shows "snap-through" behavior that is characteristic of negative stiffness materials. In contrast, the FCT structure undergoes smooth transitions under this oscillatory shear test with an absence of snap-through behavior (see Video S9 in the Supporting Information). Unfortunately, our test instrument was not capable of capturing data rapidly enough to reliably characterize these materials in oscillatory mode—yet absent the data, the videos are illustrative of the structure-dependent behavior.

To delay the onset of wall-slip, we affixed two solid skins constructed of the same ink material to both surfaces of the SC structure forming a sandwich configuration. In Figure 3b, we compare the shear stress-strain behavior for SC structures at 25% compression with and without skins. Images of the sandwiched SC structure displaying the structural deformation as the material is sheared are shown in Figure 3c–e for 0%, 40%, and 110% shear strain. Skin addition constrains the SC structure at both surfaces, yielding a more symmetric deformation under compression with delayed buckling. Therefore, the sandwiched SC structure is more efficiently pre-loaded than structures without skins, which results in earlier onset of negative slope and negative stress for a given compression. In addition, the onset of wall slip is delayed with skin addition due to increased contact area with the test fixture.

Finite element simulations offer additional insight into the negative stiffness response for the SC structure. **Figure 4**a shows engineering shear stress versus engineering shear strain for both architectures under increasing levels of pre-compression. Like the experiment, the displacement was applied to a single plate while the opposite plate remained fixed. To prevent wall-slip, the structures were fixed to the

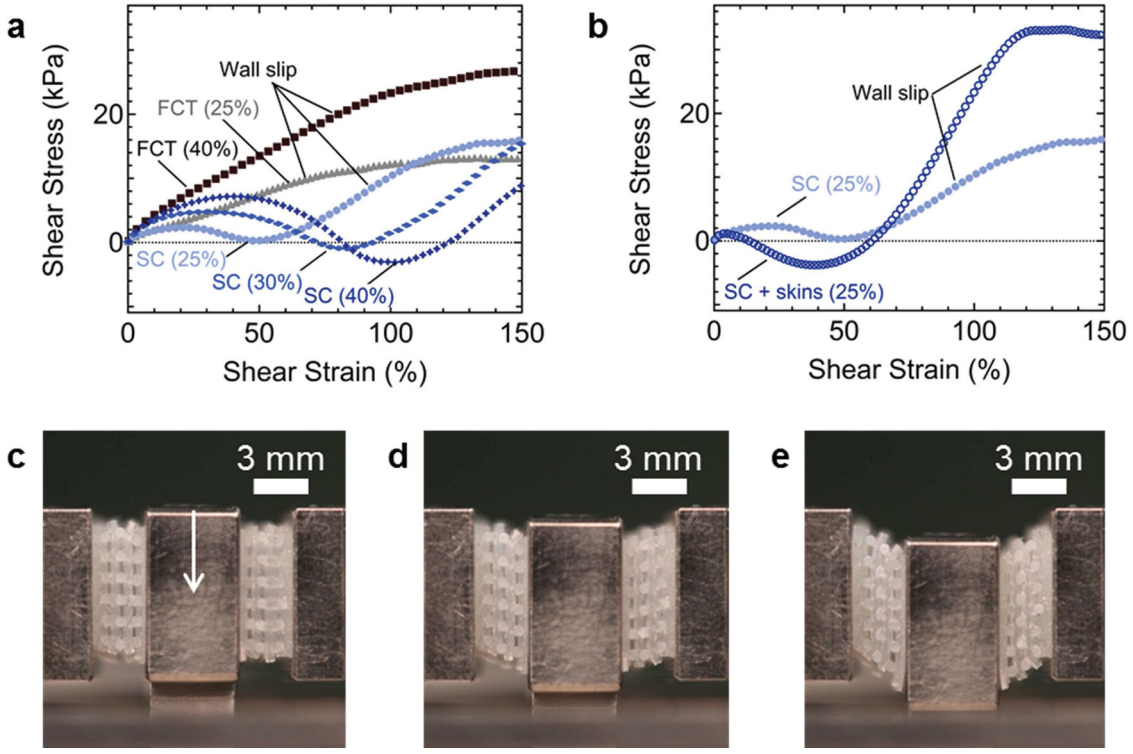

Figure 3. Architecture-dependent shear behavior. a) Experimental shear engineering stress versus shear engineering strain for SC and FCT structures at pre-compression levels indicated in parentheses. Negative shear stiffness is observed for the SC structures under pre-compression values of 25% and 35%. b) Shear stress versus shear strain comparing SC structures with and without skins at 25% pre-compression. Photographs of SC structures with skins assembled in the shear test apparatus with 25% pre-compression shown under c) 0%, d) 40%, and e) 110% shear strain.

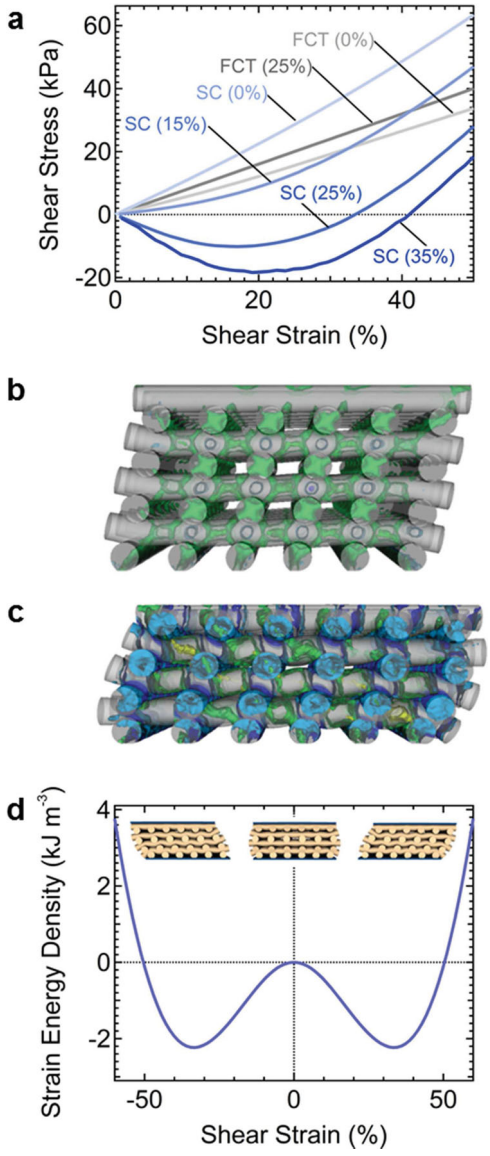

Figure 4. Finite element simulations of architecture-dependent shear behavior. a) FE shear simulations for SC and FCT structures under pre-compression levels indicated in parentheses. Negative shear stiffness is observed for the SC structure under 25% and 35% pre-compression. Side-view (*xz*-plane) of the 3D SC structure showing shear stress iso-volumes at 20% shear strain under b) 0% and c) 25% pre-compression. The iso-volumes possess bounds between –50 kPa and –20 kPa (blue), 70 kPa and 130 kPa (green), and 170 kPa and 230 kPa (yellow). The SC structure under 0% pre-compression shows clear development of "X"-shaped load paths of positive shear stress whereas the SC structure under 25% pre-compression is dominated by negative shear stress that traces compressive load column that forms under pre-compression. d) Shear strain energy density as a function of shear strain for the SC structure under 25% pre-compression showing the formation of two stable energy minima at –33% and +33% shear strain separated by a metastable region centered at 0% shear strain. Inset shows illustrations of the SC structure, from left to right, under –33%, 0%, and 33% shear strain.

plate surfaces while the edges were unconfined. With these boundary and loading conditions, the SC structure produces more stress in shear alone (i.e., without pre-compression). With pre-compression, the SC structure gradually transitions to negative stress at higher normal displacements whereas the FCT structure displays a monotonic rise in shear stress versus shear strain for all levels of compression. The difference in structure-dependent behavior can be attributed to the relative magnitudes of the shear and compressive stresses in these structures. Both architectures have a compressive/shear stiffness ratio that is greater than one, but the value for the SC structure is sufficiently high to exhibit negative stiffness under the appropriate conditions.

The origin of negative shear stiffness lies in the columnar load paths that develop under compression. When uniaxially loaded, the SC structure develops a restoring force that acts in an opposite direction to the compression. As a simple analogy, one can envision a vertical spring that is compressed. Upon initial shear movement, the spring develops a horizontal component that pushes the shear front forward as it releases the stored strain energy. With simulation, we visualize the stress patterns within the structures. In Figure 4b, c, we plot iso-volumes of shear stress in the SC architecture at 20% shear strain with 0% and 25% pre-compression, respectively. The evolution of the shear stress iso-volumes for the SC structure under 0% and 25% pre-compression while undergoing shear are also visualized in Videos S10, S11 in the Supporting Information. The blue volumes denote negative stress whereas the green, yellow, and red volumes signify increasingly positive stress. At 0% pre-compression and 20% shear strain, the green volumes are "X"-shaped, the arms of which diagonally connect adjacent filaments and are likely parallel with the principal stress directions (Figure 4b, Video S10 in the Supporting Information). In this case, negative shear stress regions are contained in smaller, isolated volumes, localized between the contact points of the upper and lower layers. With a 25% pre-compressive strain, the negative shear stress regions are much larger and exhibit connectivity throughout the vertical compressive stress columns (Figure 4c, Video S11 in the Supporting Information). In addition, the positive stress volumes are oriented only along one diagonal arm of the former "X"-shape (i.e., from upper left to lower right), corresponding to the compressive principal strain direction. In this case, the dominant negative shear stress volumes affect the topology of the positive regions, and are responsible for the negative stiffness, which is consistent with the spring analogy. At higher shear strains these negative stress regions dissipate, and the net stress eventually becomes positive.

In the experimental data, we attribute the initial positive slope at low strains to the buckling that occurs within the SC structure, which allows the filament cross-sections to expand relative to those found in a vertical load column. Consequently, the interlayer contact points become pinned, which gives rise to an internal resistance to the shear direction. As we have seen, skin addition tends to delay buckling that occurs in compression, thus creating an experimental loading condition and shear stress-strain curve shape (Figure 3b) that is more consistent with the simulations (Figure 4a). However, skin addition does not completely eliminate the initial positive slope region. Thus, there may be some small error in the SC sample loading, which could set up a small diagonal force that initially opposes the direction of shear, which would also give rise to a region

of initial positive slope. Regardless, with enough energy input into the system, the internal resistance is overcome and the filaments orthogonal to the shear direction roll past the interlayer contact points, releasing the stored strain energy and pushing the shear front forward. The result is a reduction in shear loading characterized by the negative slope in the stress-strain curve. Upon increasing shear strain, the stored energy is eventually completely released and the stress-strain slope turns positive. At even higher shear strain, the filaments aligned in the direction of shear must extend and therefore resist further deformation, eventually resulting in wall slip. The shear strain energy density versus shear strain curve for 25% pre-compression (Figure 4d) is obtained by integrating the data in Figure 4a. Note the strain energy density does not contain the 21 kJ m^{-3} of work input during the pre-compression step. In agreement with Figure 4d, Video S8 in the Supporting Information shows the SC structure snapping through the meta-stable state at 0% shear strain and adopting either of the stable minima configurations at ±33% shear strain. The location of the minima is consistent with uniaxial compression simulations that promote the instability by removing the lateral constraint on the upper plate (Figure 2d).

Based on the experimental observations and the results of the finite element simulations, we can construct a simple approximation to determine the compressive strain at which negative stiffness occurs in the SC structure. From the trends in Figure 4a, we define onset of negative stiffness as when the slope of the stress-strain curve equals zero as shear strain approaches zero. This condition requires a force balance between compression and shear so, as a first approximation, we assume $\frac{F_{\text{shear}}(\Delta x, \Delta z = 0)}{\Delta x} = \frac{F^{x}_{\text{shear}}(\Delta x, \Delta z)}{\Delta x}$, where F_{shear} is the shear force at 0% compression, F^{x}_{comp} is the compressive force component in the shear direction x, Δx is the shear displacement, and Δz is the compressive displacement. In other words, the slopes of the shear and compressive force-displacement curves must be equal as $\Delta x \to 0$. The left hand side is the force response under pure shear deformation and, for small shear, the right hand side can be approximated by $\frac{F_{\text{comp}}(\Delta x = 0, \Delta z)}{\Delta x} \sim \frac{F_{\text{comp}}\theta}{\Delta x}$, where θ is the shear angle and F_{comp} is the purely compressive force without shear. Again for small shear, $\theta \sim \tan\theta = \frac{\Delta x}{h_0 - \Delta z}$, where h^0 is the uncompressed height of the structure. Therefore the condition for the onset of negative stiffness becomes $\frac{F_{\text{shear}}}{\Delta x} = \frac{F_{\text{comp}}(\Delta z)}{h_0 - \Delta z}$, and from interpolation of the simulation data, $\epsilon_{\text{onset}} = 14\%$. This estimate only requires the response curves for pure shear and pure compression. By comparison, a more accurate value was obtained via simulation by initially shearing the SC structure by a small amount (0.5%) and then applying compression to determine at what compressive strain the normal reaction force was reduced to zero. The result was, which indicates our initial estimate was quite reasonable.

3. Conclusion

In summary, we have demonstrated the ability to independently tailor compression and shear response in 3D printed, porous elastomers via micro-architected design. Such cellular materials offer attractive alternatives to foams due to their uniformity, tunable-nature, and predictability. Further, we have demonstrated the extremal property of negative shear stiffness in SC structures. These mechanical metamaterials may find application as cushion or packaging materials with built-in load release mechanisms designed to lower stress upon reaching some threshold to prevent damage.

4. Experimental Section

Ink Preparation: Dow Corning (DC) SE1700 clear adhesive was purchased from Ellsworth Adhesives. DC SE 1700 is a two-part, thermal-cure polydimethylsiloxane adhesive with a 10:1 part A:B by weight mix ratio. In a typical preparation, we mixed 20 grams of SE 1700 part A and 2 g of part B using a Thinky planetary mixer for 30 s at 2000 rpm mix followed by 30 s at 2200 rpm de-aeration. The ink material was loaded into a 30 cc syringe barrel (Nordson) and placed in a bell jar under vacuum for 5 min for further de-aeration. Next, the 30 cc syringe was sealed with an endcap and centrifuged at 4000 rpm for 5 min. Excess air was removed by manually pressing the piston until the trapped air bleeds out. The endcap was exchanged for a micronozzle (typically 610 μm inner diameter, Nordson) and mounted to the z stage of a three-axis linear positioning system (Aerotech).

3D Printing and Post-Processing: To 3D print our micro-architectures, we first prepared a 300 mm diameter silicon wafer by coating with a PTFE mold release agent (Miller-Stephenson) and mounted this substrate to the xy stages of the positioning system. A positive displacement fluid dispenser (Ultimus IV Model 2800–30, Nordson) was attached to the syringe barrel and programmed with a displacement rate that dispensed ink at a volumetric flow rate that matched the programmed print speed (10–20 mm s^{-1}) for a 610 μm diameter nozzle. After aligning the nozzle to the substrate, a tool-path program was executed in the A3200 CNC Operator Interface Control software (Aerotech) while activating the dispense command. In a typical build, we printed 8 layers with a programmed filament center-to-center spacing of 1.22 mm for both SC and FCT patterns with a total build area of 75 mm × 75 mm. Upon completion of a part, ink dispensing was halted and the nozzle pulled away from the part surface. After printing, the silicon wafer substrate with completed part(s) was removed from the positioning system and placed in a vacuum oven (Yamato Model ADP31) purged with nitrogen gas for thermal curing at 150 °C for 60 min. Next, the wafer was removed from the vacuum oven and the silicone part was detached from the substrate.

Filler-Dependent, Isothermal Shear Moduli (G′ and G″) Characterization: DC SE1700 was blended with varying amounts of unfilled polydimethylsiloxane resin to determine the effects of filler composition on the rheological properties of uncured resin blends and on the thermomechanical properties of cured resin blends. Gelest DMS-V21 (vinyl-terminated polydimethylsiloxane, $M_w \approx 6000$ Da) and HMS-082 ((7–8% methylhydrosiloxane)-dimethylsiloxane copolymer, trimethylsiloxane-terminated, $M_w \approx 5500$ to 6500 Da) were purchased from Gelest, Inc. All materials were used as received without further purification. First, DC SE1700 was prepared according to the procedure outlined above. Next, the Gelest materials were mixed in a 1.92 to 1.00 mass ratio of DMS-V2 to HMS-082. The DC SE1700 and Gelest DMS-V21-co-HMS-082 resin mixtures were blended in 11 g batches with weight percent compositions varying from 100% to 25% DC SE1700. All sample blends were mixed using a FlackTek DAC 150 FVZ-K speed mixer using an initial mixing cycle of 1600 rpm for 30 s and an additional mixing cycle of 2400 rpm for 30 s. After mixing, the sample blends were allowed to equilibrate at ambient temperature for a period of 1 h. The mixtures were then subjected to rheological characterization to determine the effects of varying filler composition on the yield stress and viscosity of the uncured copolymer blends. Rheological properties were determined using a controlled stress AR-2000ex rheometer (TA Instruments). A cone-and-plate geometry (diameter = 40 mm, angle = 2°) was used. After an initial 1 min conditioning step using a shear rate of 0.05 s^{-1}, oscillatory stress sweep experiments were performed at room temperature (≈23°C) from 1 to 3000 Pa using a frequency of 1 Hz. Shear

rate sweep measurements were performed from 0.1–100 s^{-1}. Data were recorded and analyzed using Rheology Advantage V5.7.0 software (TA Instruments).

Time-Dependent, Isothermal Apparent Viscosity and Shear Moduli (G′ and G″): In order to investigate the time window for ink printability at room temperature, we acquired apparent viscosity versus shear rate and storage modulus versus oscillatory stress data at various time steps using a stress-controlled rheometer (AR-2000ex, TA Instruments) with a cone and plate geometry (diameter = 40 mm, angle = 2°) at room temperature (≈23°C). To mimic printing conditions and ensure each sample had the same shear history, separate 10 g ink samples were prepared for each data point using the standard ink preparation procedure. After high shear mixing, each sample was carefully loaded into the rheometer geometry and a continuous pre-shear of 1 s^{-1} was applied for a period of 1 min to achieve intimate contact between the ink and geometry surfaces. The samples were then left undisturbed for allotted times in order to observe the curing behavior at room temperature. This test condition most closely matches the actual printing process because the vast majority of ink material is in a quiescent state after loading into the syringe barrel. This state remains until the ink experiences shear forces as it reaches the micro-nozzle orifice and is extruded. To obtain the time-dependent viscosity information, a series of shear flow tests were conducted and ink apparent viscosity as a function of shear rate was acquired for each time point. In each test, the shear rate was increased from 0.1 to 100 s^{-1}. The apparent viscosity at the lowest shear rate of 0.1 s^{-1} (i.e., closest to zero rate viscosity) was plotted versus time. To obtain the time-dependent storage modulus information, a series of stress-sweep oscillatory tests were performed and storage modulus as a function of oscillatory stress was acquired for each time point. In each test, the stress was increased from 0.1 to 1000 Pa at an oscillatory frequency of 1Hz.

Rheological Characterization during Thermal Curing: The mechanical properties of the ink during thermal curing were measured using dynamic mechanical thermal analysis (DMTA). Dynamic temperature ramp tests were conducted using a parallel plate geometry (2–3 mm gap distance) on an ARES-LS2 rheometer (TA Instruments). Due to the large increase in shear storage modulus after cure, separate tests were performed using 50 and 25 mm diameter plates to best characterize the pre-cure and post-cure segments, respectively. Tests began within several minutes after mixing and the temperature was increased from 25 to 150 °C at a rate of 2 °C min^{-1} with a hold at 150 °C. Testing took place at 1 Hz oscillatory frequency. Using the auto-strain feature to keep stresses within the instrument limits, the strain ranged from 0.02–0.03% for temperatures <102 °C and 0.04–0.30% for temperatures >102 °C. The gap distance was adjusted using the auto-tension feature to maintain the compressive force on the specimen below ≈50 g as the sample cured. The shear storage and loss moduli (G' and G'', respectively) were measured.

In Situ Imaging of Structures under Compression: We investigated both SC and FCT-type lattices patterned with 610 μm diameter nozzles using a custom-built compression device while simultaneously imaging in 3D at incremental static compressions using Synchrotron Radiation micro-Tomography (SRμT). The step-wise loading procedure allowed for real-time visualization of the micro-architecture and void space during deformation. SRμT was selected due to its high resolution and high flux capabilities, which is necessary for fast acquisition imaging of a large sample volume while still producing micrometer spatial resolution. The tomographic imaging was performed at beamline 8.3.2 at the Advanced Light Source (Lawrence Berkeley National Laboratory, Berkeley, CA, USA) in monochromatic mode at an energy of 16 keV. The setup was similar to standard tomographic procedures.[38] The sample was rotated 180° in an X-ray beam and the transmitted radiographic projections (1025 images total per data set) were imaged via a scintillator, magnifying lens, and a digital camera to give an effective voxel size of 9 μm^3. The reconstructed images were obtained via a filtered back projection algorithm. Each data set was reconstructed using the software Octopus (inCT) and the 3D visualization and quantification of void distribution was performed using Avizo software (FEI Visualization Sciences Group).

Uniaxial Compression Testing: Compression testing was carried out on an Instron Electropuls E10000 All Electric Test System equipped with a 2.868 cm diameter lower fixture plate and an oversized upper plate at room temperature (≈23 °C). Testing was carried out in a cyclic mode comprised of loading and unloading cycles. At the start of the first loading step, the test was started with an air gap and compression proceeded at a crosshead speed of 1.26 mm min^{-1}. Loading proceeded until a stress of 2000 kPa was achieved, at which time unloading was immediately started, again at a crosshead speed of 1.26 mm min^{-1} until a stress of 0 kPa was achieved. This process was repeated three cycles at a given test location. Four non-overlapping locations were evaluated on each 8 layer, 75 mm × 75 mm part with four parts tested for both FCT and SC structures. The results for these tests were corrected for machine compliance and the quantities of engineering compressive strain and engineering compressive stress were calculated by known formulas. The thickness used to calculate strain is based on the thickness at which the compressive stress reached 2 kPa on the first loading step.

Shear Behavior under Applied Axial Compression: To determine the shear behavior of our printed cellular materials under applied pre-compressive strain conditions, shear sandwich characterization experiments were performed using a TA Instruments Q800 dynamic mechanical analyzer on 8 layer samples printed with 610 μm nozzles. All samples were diced into ≈6 mm × 6 mm sample sizes in xy dimensions from larger 75 mm × 75 mm parts. For each sample, axial strains of 15%, 25%, 40%, and 55% were applied by calculating the appropriate thicknesses for each sample for each strain value and compressing each sample axially using calipers to measure sample thickness. All shear sandwich experiments were run at room temperature (≈23 °C). To determine the storage modulus of printed samples under varying levels of applied axial strain, dynamic strain sweep experiments were run in the DMA Multi-Strain mode using a logarithmic displacement range of 1 to 3000 μm with 10 points per decade at a frequency of 1 Hz. To determine the internal stresses on the samples at varying levels of applied axial strain as shear strain is increased in a linear manner, controlled shear strain ramp experiments were run in the DMA Strain Rate mode using a shear strain range of 0 to 200% strain and a displacement rate of 20% strain per minute. These shear strain ramp experiments were run to generate plots of shear stress versus shear strain for each sample under varying axial deformation conditions.

Finite Element Simulation: Finite element simulations were performed with the NIKE3D implicit solver. NIKE3D is a nonlinear, implicit, 3D finite element code for solid and structural mechanics developed at Lawrence Livermore National Laboratory. The domains consisted of 8 layers of 610 μm diameter elastomeric circular filaments with variable spacing and alternating orientations corresponding to the SC and FCT geometries. For the compression simulations of the ideal structures, each layer contained three filaments and symmetric boundary conditions were applied on the lateral boundaries. In the overlapped structure simulations for compression only and compression followed by shear, the interlayer center-to-center spacings were 0.85D and 0.8D, respectively, where D is the filament diameter. Each layer contained six filaments and the symmetric boundary conditions were removed. Two thin plates of a stiff material bounded the upper and lower regions of the domain and provided loading and additional constraints for the simulations; a linear displacement was applied to the upper plate while the lower one remained fixed. The overlapped structures were tied to both plates. The mesh for each micro-architecture contained approximately 1.2 million hexahedral elements with sizes ranging from 0.08 to 0.25D. The simulations advanced through a series of static loading steps, during which a fixed displacement was applied and the resulting equilibrium configuration was computed through an iterative solver. The displacement step size was automatically adjusted to minimize the number of iterations while satisfying the convergence criteria. Measurement of the reactive force on the upper plate provided the stress response data. The materials model for the simulations was derived from experimental compression measurements of a cylindrical specimen of the bulk SE1700 material. The stress response curve was fit to a Mooney-Rivlin constitutive equation using a least squares approach

to determine the two coefficients. To avoid complications arising from compression set from the Mullins effect, we fit the data from the third cycle from the applied loading.

Supporting Information

Supporting Information is available from the Wiley Online Library or from the author.

Acknowledgements

E.B.D. and T.H.W. contributed equally to this work. The authors thank Charles Anderson, Matt Lampe, and Dan Bowen at Kansas City Plant for useful discussions. The authors acknowledge Michael Puso, Ian Darnell, and Robert Ferencz for helpful discussions on implementing the NIKE3D software. The authors acknowledge the photograph in Figure 1a by Jamie Douglas. The authors thank Mark Pearson for assistance with mechanical testing. The authors also acknowledge Scott Fisher for design and assembly of the in situ compression apparatus for SRμT imaging. The authors acknowledge the use of the Synchrotron Radiation micro-Tomography beam-line (8.3.2) at the Advanced Light Source (ALS) at Lawrence Berkeley National Laboratory. The ALS is supported by the Director, Office of Science, Office of Basic Energy Sciences, of the U.S. Department of Energy under Contract No. DE-AC02–05CH11231. The authors also thank Prof. Duncan J. Maitland at Texas A&M University for volunteering the use of the TA Instruments Q800 Dynamic Mechanical Analyzer for the shear sandwich DMA experiments reported in this study. The authors also thank Sean Kohl and TA Instruments for kindly volunteering the use of the Q800 shear sandwich clamps used in the shear sandwich DMA experiments in this study. This work was funded by the Laboratory Directed Research and Development Strategic Initiative program, 11-SI-005, and performed under the auspices of the U.S. Department of Energy by Lawrence Livermore National Laboratory under Contract No. DE-AC52–07NA27344 with IM Review No. LLNL-JRNL-646053.

Received: February 10, 2014
Published online: May 2, 2014

[1] A. G. Evans, J. W. Hutchinson, N. A. Fleck, M. F. Ashby, H. N. G. Wadley, *Prog. Mater. Sci.* **2001**, *46*, 309.
[2] L. J. Gibson, M. F. Ashby, *Cellular Solids: Structure and Properties* 2nd ed., Cambridge University Press, Cambridge **1997**.
[3] J.-H. Lee, J. P. Singer, E. L. Thomas, *Adv. Mater.* **2012**, *24*, 4782.
[4] T. Bückmann, N. Stenger, M. Kadic, J. Kaschke, A. Frölich, T. Kennerknecht, C. Eberl, M. Thiel, M. Wegener, *Adv. Mater.* **2012**, *24*, 2710.
[5] V. S. Deshpande, N. A. Fleck, M. F. Ashby, *J. Mech. Phys. Solids* **2001**, *49*, 1747.
[6] V. S. Deshpande, M. F. Ashby, N. A. Fleck, *Acta Mater.* **2001**, *49*, 1035.
[7] Y. C. Wang, R. S. Lakes, *Am. J. Phys.* **2004**, *72*, 40.
[8] R. Lakes, *Science* **1987**, *235*, 1038.
[9] S. Babaee, J. Shim, J. C. Weaver, E. R. Chen, N. Patel, K. Bertoldi, *Adv. Mater.* **2013**, *25*, 5044.
[10] K. Bertoldi, P. M. Reis, S. Willshaw, T. Mullin, *Adv. Mater.* **2010**, *22*, 361.
[11] J. Shim, C. Perdigou, E. R. Chen, K. Bertoldi, P. M. Reis, *Proc. Natl. Acad. Sci.* **2012**, *109*, 5978.
[12] R. S. Lakes, T. Lee, A. Bersie, Y. C. Wang, *Nature* **2001**, *410*, 565.
[13] B. Moore, T. Jaglinski, D. S. Stone, R. S. Lakes, *Philos. Mag. Lett.* **2006**, *86*, 651.
[14] R. S. Lakes, *Philos. Mag. Lett.* **2001**, *81*, 95.
[15] I. Gibson, D. W. Rosen, B. Stucker, *Additive Manufacturing Technologies: Rapid Prototyping to Direct Digital Manufacturing*, Springer, New York **2010**.
[16] J. A. Lewis, *Adv. Funct. Mater.* **2006**, *16*, 2193.
[17] J. N. Hanson Shepherd, S. T. Parker, R. F. Shepherd, M. U. Gillette, J. A. Lewis, R. G. Nuzzo, *Adv. Funct. Mater.* **2011**, *21*, 47.
[18] S. J. Hollister, *Nat. Mater.* **2005**, *4*, 518.
[19] D. Therriault, S. R. White, J. A. Lewis, *Nat. Mater.* **2003**, *2*, 265.
[20] W. Wu, C. J. Hansen, A. M. Aragon, P. H. Geubelle, S. R. White, J. A. Lewis, *Soft Matter* **2010**, *6*, 739.
[21] J. S. Miller, K. R. Stevens, M. T. Yang, B. M. Baker, D.-H. T. Nguyen, D. M. Cohen, E. Toro, A. A. Chen, P. A. Galie, X. Yu, R. Chaturvedi, S. N. Bhatia, C. S. Chen, *Nat. Mater.* **2012**, *11*, 768.
[22] K. S. Toohey, N. R. Sottos, J. A. Lewis, J. S. Moore, S. R. White, *Nat. Mater.* **2007**, *6*, 581.
[23] N. G. Durmus, S. Tasoglu, U. Demirci, *Nat. Mater.* **2013**, *12*, 478.
[24] M. Deubel, G. von Freymann, M. Wegener, S. Pereira, K. Busch, C. M. Soukoulis, *Nat. Mater.* **2004**, *3*, 444.
[25] E. B. Duoss, M. Twardowski, J. A. Lewis, *Adv. Mater.* **2007**, *19*, 3485.
[26] G. M. Gratson, F. García-Santamaría, V. Lousse, M. Xu, S. Fan, J. A. Lewis, P. V. Braun, *Adv. Mater.* **2006**, *18*, 461.
[27] F. García-Santamaría, M. Xu, V. Lousse, S. Fan, P. V. Braun, J. A. Lewis, *Adv. Mater.* **2007**, *19*, 1567.
[28] M. S. Rill, C. Plet, M. Thiel, I. Staude, G. von Freymann, S. Linden, M. Wegener, *Nat. Mater.* **2008**, *7*, 543.
[29] T. Ergin, N. Stenger, P. Brenner, J. B. Pendry, M. Wegener, *Science* **2010**, *328*, 337.
[30] B. Y. Ahn, E. B. Duoss, M. J. Motala, X. Guo, S.-I. Park, Y. Xiong, J. Yoon, R. G. Nuzzo, J. A. Rogers, J. A. Lewis, *Science* **2009**, *323*, 1590.
[31] J. J. Adams, E. B. Duoss, T. F. Malkowski, M. J. Motala, B. Y. Ahn, R. G. Nuzzo, J. T. Bernhard, J. A. Lewis, *Adv. Mater.* **2011**, *23*, 1335.
[32] K. Sun, T.-S. Wei, B. Y. Ahn, J. Y. Seo, S. J. Dillon, J. A. Lewis, *Advanced Materials* **2013**. *25*, 4539.
[33] A. J. Jacobsen, W. Barvosa-Carter, S. Nutt, *Acta Mater.* **2007**, *55*, 6724.
[34] A. J. Jacobsen, W. Barvosa-Carter, S. Nutt, *Adv. Mater.* **2007**, *19*, 3892.
[35] T. A. Schaedler, A. J. Jacobsen, A. Torrents, A. E. Sorensen, J. Lian, J. R. Greer, L. Valdevit, W. B. Carter, *Science* **2011**, *334*, 962.
[36] D. Jang, L. R. Meza, F. Greer, J. R. Greer, *Nat. Mater.* **2013**, *12*, 893.
[37] L. Mullins, *Rubber Chem. Technol.* **1969**, *42*, 339.
[38] J. H. Kinney, M. C. Nichols, *Ann. Rev. Mater. Sci.* **1992**, *22*, 121.